Complex Fluorine Chemical Potential Effects on the Shape and Compositional Heterogeneity of KTa$_{1-x}$Nb$_x$O$_3$ Nanoparticles

Tiffany Ly, Jianguo Wen, and Laurence D. Marks*

ACCESS | 📊 Metrics & More | 📖 Article Recommendations | 🆂🅸 Supporting Information

ABSTRACT: When kinetic conditions dominate and dictate the growth in a nanoparticle synthesis, properties of the synthesis environment can have considerable effects on the properties of the products. Such effects were studied here, where the solution environment was changed via the addition of KF to the hydrothermal syntheses of KTa$_{1-x}$Nb$_x$O$_3$ and KTaO$_3$. One result demonstrated the straightforward cause-and-effect relationship between the solution and reaction kinetics: KF directly increased the solution stability of the Ta species and therefore decreased its reaction rate, resulting in a change in composition heterogeneity of Ta and Nb in the KTa$_{1-x}$Nb$_x$O$_3$ particles. However, not all effects are so simple; changing the chemical potential of the solution with KF can also promote the formation of particles with anisotropic defect enhanced kinetic Wulff shapes instead of cuboidal shapes. The increased F chemical potential in the solution enabled the formation of planar defects in the bulk, which accelerated growth in-plane to form particles characterized by flat rectangular flake geometries. Thermodynamic modeling with density functional theory calculations confirmed that sufficient KF concentrations can drive the formation of a defect phase K$_{n+1}$Ta$_n$O$_{3n}$F.
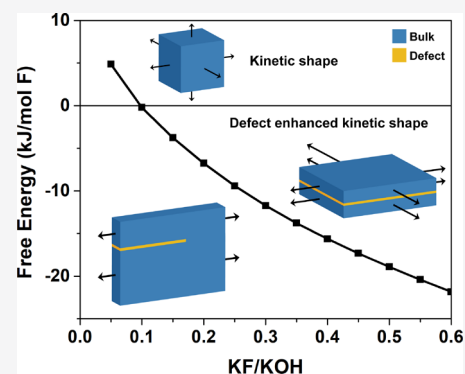
INTRODUCTION

The thermodynamic Wulff construction, defined by the minimization of surface energy of a crystal, establishes the equilibrium shape of a nanoparticle;[1] however, this is only valid under equilibrium conditions where there is enough time and energy for the diffusion processes to form the minimum energy shape. In many nanoparticle syntheses, especially solution-based methods, equilibrium conditions are uncommon and except for diffusion-controlled cases, kinetic conditions dominate instead. In the kinetic limit, the shape of the nanoparticles, termed as the kinetic Wulff shape, is determined by the growth rates of different facets rather than their surface energies.[2−8] Part of the difficulty in understanding and predicting kinetic Wulff shapes is the complexity in how many different factors can control different properties and rates of growth, which is why it is prudent to identify key regions and their relevant thermodynamic and kinetic properties. For the solution-based hydrothermal syntheses that are the focus of this work, these key regions are depicted schematically in Figure 1 as region I, the aqueous solution; region II, the near surface region where species are interacting with the particle surface; region III, the particle surface where growth occurs; and region IV, the bulk where defects such as stacking faults and twin boundaries can enhance growth in particular directions.[9−14]

The roles of several of these regions in the synthesis of KTa$_{1-x}$Nb$_x$O$_3$ (x = 0−1) (KTN) materials have already been analyzed through previous studies. For instance, it was demonstrated in the hydrothermal synthesis of KTaO$_3$
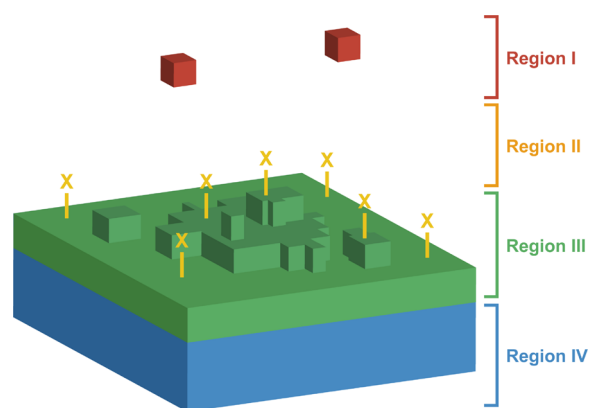

Figure 1. Schematic of key regions for solution-based nanoparticle growth. Region I is the solution, which includes all dissolved active and inactive species. Region II encompasses the near surface region where species in the solution interact with the growing surface, such as via chemisorption. Region III contains the growing surface. Region IV is the bulk, where bulk defects can form and affect growth.

(KTO) that the relative kinetics of the step-flow growth mechanisms in Region III were controlled by the changing thermodynamic properties of Region I over the course of the synthesis reaction.[15] Regions I, II, and III may also all be interlinked; when the growth of KTN nanoparticles with different surface chemistries (Ta or Nb), which could be controlled by their relative stabilities in region I, were compared, it was shown that the chemisorption behavior in region II could impact the growth morphology in region III.[16]

The relationships between regions I and IV and their effects on KTN and KTO particles are the focus of this study. Potassium fluoride was added to the aqueous hydrothermal solution to affect the relative solution stabilities of the reagents during reaction and to act as a driving force behind the formation of bulk planar defects in the produced materials. Changes in the relative solution stabilities of the reagents directly affected their reaction rates, and therefore, the composition of the products. Density functional theory and thermodynamic calculations were also used to model the more complex results caused by the increased solution chemical potential from the addition and potential incorporation of KF. These calculations confirmed that the experimental conditions were sufficient for forming Ruddlesden−Popper-like planar bulk defects in the particles. These defects promoted the formation of a defect enhanced kinetic Wulff shape by breaking the cubic symmetry of the perovskite structure and accelerating growth along the directions of the defect, resulting in anisotropic rectangular flakes.

■ METHODS

All of the nanoparticle samples were grown using a hydrothermal synthesis adapted from Goh et al.,[17] where 0.0025 mol M_2O_5 (M = Ta and/or Nb), 25 mL 15 M KOH, and different amounts of KF were added to a 125 mL Teflon-lined autoclave, heated to 200 °C for 1−12 h. The molar ratio KF/KOH was varied between 0.15 and 0.35. After cooling to room temperature, the product was washed several times with deionized water and dried overnight at 80 °C.

Powder X-ray diffraction (XRD) was used to characterize the yielded phases of each synthesis. XRD was performed on a Rigaku Ultima diffractometer and Smartlab 3 kW Gen2 operated at 40 kV and 44 mA. Electron microscopy was performed on a Hitachi HD-2300 STEM and FEI Talos F200X TEM/STEM operated at 200 kV. Argonne chromatic aberration-corrected TEM (ACAT), an FEI Titan with a CEOS C_c/C_s image corrector at Argonne National Laboratory, was used to perform high-resolution transmission electron microscopy (HRTEM). MacTempasX software package,[18] which uses the multislice method[19] and nonlinear imaging theory,[20] was used to simulate HRTEM images.

Density functional theory calculations were done using WIEN2k, an augmented plane wave plus local orbital code,[21−23] with the PBEsol functional.[24] The muffin tin radii (RMT) were set to 2.26, 1.8, 1.72, 1.56, and 1.63 for K, Ta, Nb, O, and F, respectively, and the RKmax was set to 7. A k-point mesh of 7 × 7 × 7 and 9 × 9 × 9 were used for the perovskite and KF structures, respectively. For the Ruddlesden−Popper defect structures, the k-point mesh was set to 8 × 8 × 8 (n = 1 and 2) and 7 × 7 × 1 (n = 3).

■ RESULTS

A series of KTN nanoparticles were synthesized with increasing concentrations of KF to determine any critical concentrations for kinetic changes in the synthesis. XRD patterns acquired for each sample confirm the formation of the perovskite phase (Figure 2a). The reaction kinetics were
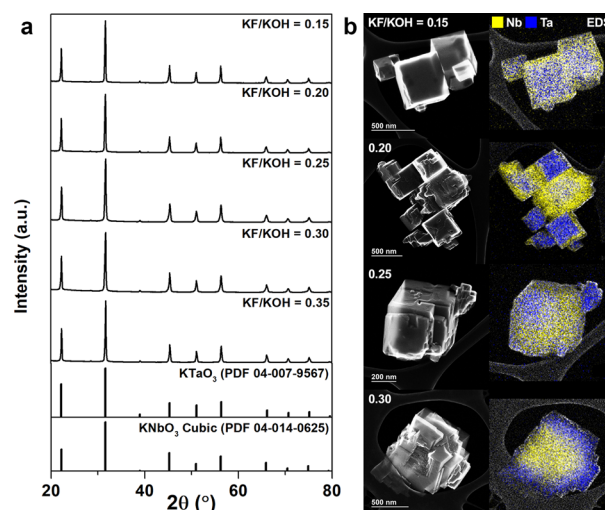

Figure 2. (a) Powder XRD patterns of KTN particles synthesized with KF/KOH = 0.15−0.35. All samples matched well to the perovskite phases KTO (PDF 04-007-9567) and KNO (PDF 04-014-0625). (b) SE images of nanocuboidal KTN particles synthesized with KF/KOH = 0.15-0.30. Corresponding EDS maps show different composition distributions of Nb (yellow) and Ta (blue) as KF/KOH increased.

related to the composition distribution of tantalum and niobium in the particles, as shown in the secondary electron (SE) images and corresponding energy dispersive X-ray spectroscopy (EDS) maps in Figure 2b. The distributions of niobium (yellow) and tantalum (blue) were not homogeneous across the entire series, and the interior bulk composition corresponded to the species with the higher reaction rate while the exterior surface composition corresponded to the slower reacting species. At low KF concentrations (KF/KOH < 0.25), the particles had a tantalum-rich interior and a niobium-rich surface. Higher concentrations of KF caused the composition to invert; the bulk became niobium-rich and the surface became tantalum-rich. This inversion confirms that the reaction kinetics between KOH and the niobium and tantalum oxides to forming the final KTN perovskite phase could indeed be controlled by a critical concentration of KF.

Significant morphology changes corresponding to increasing KF/KOH concentrations were also observed. The nano-cuboids shown in Figure 2 were typical of particles grown at lower KF/KOH concentrations, and their morphologies matched the nucleation and growth via surface terraces behavior studied previously.[15,16] In contrast to the nano-cuboids, anisotropically shaped particles also formed at higher concentrations of KF (KF/KOH > 0.20). These particles were flat rectangular flakes on the order of several hundred nanometers wide and ~100 nm thick (Figure 3), and EDS maps of these particles shown in Figure S1 did not demonstrate any significant composition segregation as the cuboidal KTN particles did. While the formation of geometrically anisotropic KTN particles would not be unusual for the
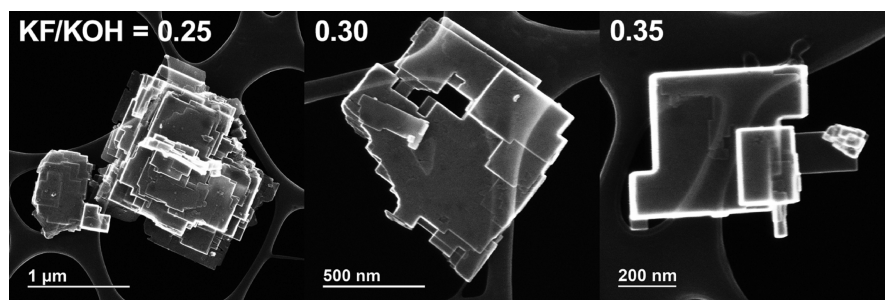
Figure 3. SE images of KTN particles synthesized with KF/KOH = 0.25−0.35. Particles exhibit rectangular flake geometries ∼100 nm thick.

material because KNO is polymorphic, KTO is an incipient ferroelectric that remains at cubic to low temperatures. Anisotropic rod-like KNO particles have been produced with hydrothermal synthesis, commonly of the tetragonal and orthorhombic KNO phases.[25,26]

As a cubic material, this result would be unexpected in KTO and would imply a breaking of the cubic symmetry. To investigate further, KTO was synthesized with two different KF/KOH ratios (0.20 and 0.30) below and above the concentrations where composition inversion in the KTN samples occurred. Two different reaction times were used in each case: a shortened time period (1 h) to capture the nucleation morphology after an incubation period and a longer time period to compare the particle morphologies after the growth period. As shown in Figure 4, the morphologies of the
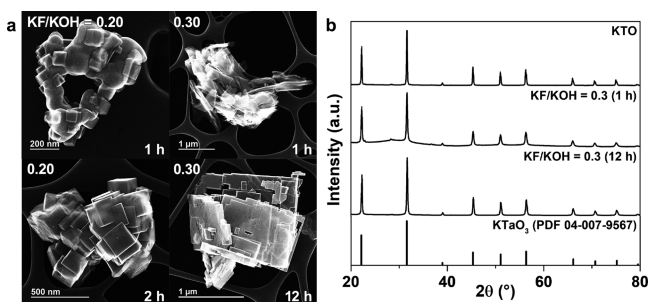

Figure 4. (a) SE images of KTO synthesized with different KF/KOH ratios after different reaction times. When KF/KOH = 0.2 (left column), particles were nucleated with cuboidal morphology (1 h) and subsequently continued to grow into larger nanocuboids (2 h). When KF/KOH = 0.3 (right column), particles nucleated with irregular flake morphologies (1 h) and grew into large rectangular flakes (12 h). (b) XRD patterns of KTO synthesized with KF/KOH = 0 for 4 h and KF/KOH = 0.30 for 1 and 12 h. All samples matched the KTO perovskite phase (PDF 04-007-9567).

particles nucleated and grown under the two KF/KOH ratios differed greatly. When KF/KOH = 0.20, the cuboidal morphology persisted after nucleation (1 h) and growth (2 h) as expected. Conversely, when KF/KOH = 0.3, the particles nucleated as irregular flakes (1 h) that subsequently grew into large rectangular flakes (12 h). XRD patterns of the two samples grown with KF/KOH = 0.30 are compared with a standard KTO sample synthesized with no KF in Figure 4b. They confirm that the cubic perovskite KTO phase (PDF 04-007-9567) was formed in all cases. The broad amorphous peak at 30° in the 1 h XRD pattern indicated that not all the tantalum oxide was reacted, suggesting a slowed reaction rate.

Since the structure remains cubic, there had to be some other explanation of the change in morphology. As mentioned

in the Introduction, bulk defects (Region IV) can lead to enhanced growth in certain directions, i.e., defect-enhanced kinetic Wulff shapes. To explore this further, the structure of the KTO rectangular flakes were characterized with TEM to identify defects that could cause this growth behavior. The high contrast in the bright field (BF) image of a particle oriented on the [113] zone in Figure 5a shows that the
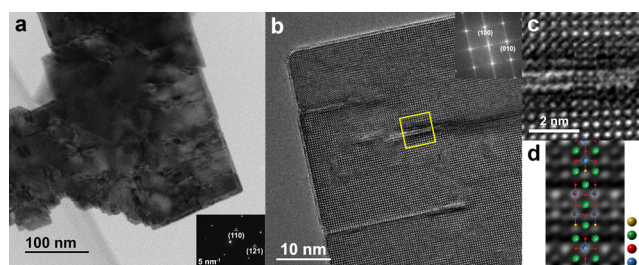

Figure 5. (a) BF image of the KTO particle on [113] zone axis. Particle shows strain contrast arising from planar defects. (b) HRTEM image and corresponding FFT of the KTO particle on [001] zone axis with several defects. The defect outlined by the yellow box is enlarged in (c), showing contrast matching a Ruddlesden−Popper-like planar defect. A multislice HRTEM image simulation of the defect structure is inset. (d) Image simulation with a Ruddlesden−Popper-like unit cell (n = 2) superimposed. Yellow atoms are F, green atoms are K, red atoms are O, and blue atoms are Ta.

particles were highly strained, which agrees with the fact that these particles were not grown under thermodynamic equilibrium conditions. The HRTEM image in Figure 5b shows a particle oriented along the [001] zone. When imaged along this zone, most of the contrast is localized around defects, implying that the defects had planar geometries oriented along the {001} planes of the material. One of the defects, highlighted by a yellow rectangle, is enlarged in Figure 5c. This defect shows misalignment of the lattice planes and contrast characteristic of a Ruddlesden−Popper-like shift between perovskite layers. A multislice HRTEM image of a defect Ruddlesden−Popper-like structure is inset into the image in Figure 5c and enlarged in Figure 5d where the unit cell is superimposed.

The Ruddlesden−Popper (RP) phase is a perovskite-type structure with interwoven layers of perovskite-like slabs with the general formula $A_{n+1}B_nX_{3n+1}$. Anion substitution for oxygen with fluorine is common in oxides,[27−29] and RP-like layer defects have been observed in ABO_3 perovskite oxides.[30−33] X-ray photoelectron spectroscopy was used to confirm the incorporation of F into the oxide. (Supporting Information) DFT calculations were used in combination with experimental
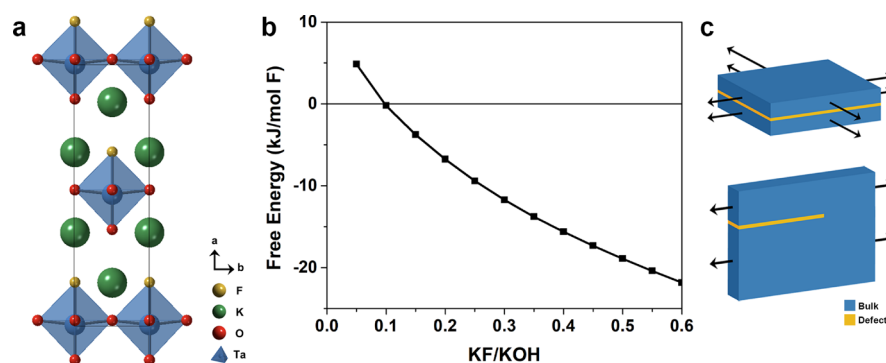
Figure 6. (a) RP-like $K_{n+1}Ta_nO_{3n}F$ ($n = 1$) unit cell used for DFT calculations. Yellow atoms are F, green atoms are K, red atoms are O, and blue octahedra are Ta. (b) $\Delta G_{total}(n = 1-3)$ normalized per mol F calculated for different KF/KOH. When normalized, $\Delta G_{total}(n = 1-3)$ all fall on the same line where the free energy is negative when KF/KOH > 0.10. (c) Schematics of accelerated growth directions in the presence of planar defects (yellow).

thermodynamic terms to calculate the formation energy of an RP-like $K_{n+1}Ta_nO_{3n}F$ ($n = 1-3$) defect phase and assess its feasibility under the experimental synthesis conditions. The relaxed crystal structure of the lowest energy RP-like unit cell for $n = 1$ is shown in Figure 6a with (KF:KO) RP-like rock salt interwoven layers between perovskite slabs. The following reaction equation was considered to compare the relative energies of forming $K_{n+1}Ta_nO_{3n}F$ versus the perovskite (KTO)

$$n \text{ KTaO}_3 + \text{KF} \rightleftharpoons K_{n+1}Ta_nO_{3n}F \qquad (1)$$
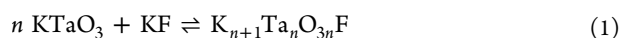
The total free energy change (ΔG_{total}) was calculated as

$$\Delta G_{total} = \Delta G_{reaction} - \Delta \mu_{KF} \qquad (2)$$

where $\Delta G_{reaction}$ is normalized per mol F to compare the relative formation energies for $n = 1-3$:

$$\Delta G_{reaction} = \frac{1}{5n + 2}(\Delta G_{K_{n+1}Ta_nO_{3n}F} - n \Delta G_{KTaO_3} - \Delta G_{KF}) \qquad (3)$$

where $\Delta G_{K_{n+1}Ta_nO_{3n}F}$ is the Gibbs free energy of the RP-like defect material, ΔG_{KTaO_3} is the Gibbs free energy of bulk KTaO$_3$, and ΔG_{KF} is the Gibbs free energy of KF. $\Delta \mu_{KF}$ is defined as:

$$\Delta \mu_{KF} = 2RT\ln(m \gamma(m)) \qquad (4)$$

where R is the gas constant, T is the temperature, m is the molality of KF in the aqueous solution, and $\gamma(m)$ is the mean ionic activity coefficient for KF, which varies with concentration.[34] Equation 3 was calculated with DFT, and eq 4 was calculated using literature tables.[35,36] Additional information about these calculations is provided in the Supporting Information. The total free energy change of the reaction is plotted in Figure 6b at different KF/KOH molar ratios, demonstrating that when KF/KOH > 0.10, $K_{n+1}Ta_nO_{3n}F$ may form. Enhanced growth due to these defects, such as the examples drawn in Figure 6c, is thus the source of the symmetry breaking.

DISCUSSION

In comparison to the change in shape at high concentrations of KF due to defect-enhanced growth, the cause of the more subtle changes at lower concentrations is more clearly isolated to solution effects. To fully understand these, the differences between tantalum and niobium chemistry must be also understood. The difference in reaction rates between KOH

and the metal oxides, Nb_2O_5 and Ta_2O_5, to form KTN perovskite nanoparticles were compared in a previous study. It was shown that the composition gradient could be inverted from having a tantalum-rich interior and a niobium-rich surface to a niobium-rich interior and a tantalum-rich surface by pre-dissolving niobium oxide in a basic KOH solution before hydrothermal synthesis.[16] However, the same niobium oxide dissolution procedure could not be replicated with tantalum oxide. The inverted Ta−Nb composition gradient effect was mirrored here by the addition of high concentrations of KF (Figure 2), which implied that the KF, or more specifically the fluoride, similarly affected the dissolution of the oxides in solution. The solubility of niobium oxides and insolubility of tantalum oxides have been studied in the literature, commonly using the Lindqvist ion ($M_6O_{19}^{8-}$) and its different types of oxygen sites as models for explaining the metal oxide dissolution behavior.[37-41] Protonation is an important step toward oxide dissolution, and the more basic bridging oxygen site in $Nb_6O_{19}^{8-}$ increases its proton affinity, while the more basic oxygen site in $Ta_6O_{19}^{8-}$ is terminal oxygen, which is a less stable protonation site.[38]

Substitution of oxygen atoms with fluorine can change these properties. A study of tantalum fluoride complexes showed that most of these complexes are composed of bridging oxygens and terminal fluorine atoms.[42] Because the terminal oxygen sites were determinative in the solubility of tantalum oxide, if the terminal oxygen is substituted with fluorine, which has a higher proton affinity than oxygen, then the stability of the protonation site can increase. Increased protonation stability increases the solubility of the oxide and thereby increases the stability of that dissolved species in solution. A more stable species in solution is less energetically favored to react, which can explain the observations in the KTN particles synthesized with KF. Increasing concentrations of F ions in solution increased the stability of the tantalum species in solution, which decreased its reactivity, and therefore, the reaction rate. At high enough concentrations, this reaction rate was slowed enough to result in a composition inversion because the rate of the reaction of the niobium species was higher.

The composition changes in the KTN particles were caused by KF catalyzed changes to reaction kinetics, and similarly, the appearance of rectangular flake-shaped KTN and KTO particles can be explained by growth kinetic changes driven by the chemical potential of KF in solution. DFT and thermodynamic calculations demonstrated that when KF/

KOH > 0.10, an RP-like oxide structurally similar to a planar defect could be formed through the incorporation of fluorine into the particles. If a planar defect forms in a crystal, it can kinetically enhance the growth of a particle adjacent to the defect. The driving force of formation is increased by higher KF concentrations, and experimentally, the rectangular flakes were produced when KF/KOH > 0.20. Kinetically enhanced growth at twins and stacking faults have been characterized in the literature in many nanoparticles, which in some cases has resulted in a variety of flat plate-like particles in many materials.[7,9−14] Growth is enhanced at those sites because of more favorable local coordination of atoms along the plane of the planar defects.

The TEM images in Figure 5 showed the structural characteristics of the planar defects. In general, the RP-like defects formed aligned to the {001} faces of the particles and accelerated growth along the plane of the defect. This directional kinetic enhancement resulted in the rectangular flakes imaged in Figures 3−5. In addition, the varying defect sizes and contrasts shown in the TEM images indicated that the defects were relatively nonuniform and often not simple single plane defects. Variations in the excess fluorine incorporated in the material can affect the size and structure of the defects. For example, the defect highlighted and simulated in Figure 5c structurally matched an RP-like defect with $n = 2$, but the formation of the RP-like $K_{n+1}Ta_nO_{3n}F$ oxide defect with $n = 1$ or 3 (even $n > 3$) is also equally, energetically likely based upon the formation energies shown in Figure 6. It is also important to note that in addition to the rectangular flakes, KTO and KTN nanocuboids were also grown in all samples even in solutions with high KF/KOH. The variation in kinetic Wulff shapes suggested that these hydrothermal syntheses had mixed growth control between different kinetic conditions, and that continuing variations in $\Delta\mu_{KF}$ as the reaction progressed contributed to the variety of particle shapes and nonuniform defects formed.

CONCLUSIONS

In modeling nanoparticle synthesis, it is critical to understand the role of different experimental conditions on the kinetics of reactions and growth to understand and accurately predict outcomes. KF played several roles in the synthesis and growth of KTN and KTO particles. In the solution (Region I), fluoride ions increased the solution stability of Ta species and decreased its rate of reaction to forming the perovskite. Because Ta reacted slower than the Nb species, this resulted in a composition gradient inversion in KTN nanoparticles produced when KF/KOH > 0.20. As demonstrated experimentally and modeled thermodynamically, KF was also incorporated into the particles as RP-like planar defects (Region IV). These planar defects accelerated anisotropic growth and resulted in the growth of defect enhanced kinetic Wulff shaped particles characterized by their large, flat rectangular flake geometries.

ASSOCIATED CONTENT

ⓈⒾ Supporting Information

The Supporting Information is available free of charge at https://pubs.acs.org/doi/10.1021/acs.jpcc.0c07517.

Additional information including EDS maps of the KTN particles, X-ray photoelectron spectroscopy character-

ization of the samples, and details of the DFT calculations (PDF)

AUTHOR INFORMATION

Corresponding Author

Laurence D. Marks − *Department of Materials Science and Engineering, Northwestern University, Evanston, Illinois 60208, United States*; Email: l-marks@northwestern.edu

Authors

Tiffany Ly − *Department of Materials Science and Engineering, Northwestern University, Evanston, Illinois 60208, United States*; ⓞ orcid.org/0000-0002-8675-1467

Jianguo Wen − *Center for Nanoscale Materials, Argonne National Laboratory, Lemont, Illinois 60439, United States*; ⓞ orcid.org/0000-0002-3755-0044

Complete contact information is available at:
https://pubs.acs.org/10.1021/acs.jpcc.0c07517

Notes

The authors declare no competing financial interest.

REFERENCES

(1) Wulff, G. On the Question of Speed of Growth and Dissolution of Crystal Surfaces. *Z. Kristallogr.* **1901**, *34*, 449−530.

(2) Berg, W. F. Crystal Growth from Solutions. *Proc. R. Soc. London, Ser. A* **1938**, *164*, 79−95.

(3) Burton, W. K.; Cabrera, N.; Frank, F. C. The Growth of Crystals and the Equilibrium Structure of Their Surfaces. *Philos. Trans. R. Soc., A* **1951**, *243*, 299−358.

(4) Bircumshaw, L. L.; Riddiford, A. C. Transport Control in Heterogenous Reactions. *Q. Rev., Chem. Soc.* **1952**, *18*, 157−1666.

(5) Winn, D.; Doherty, M. F. Modeling Crystal Shapes of Organic Materials Grown from Solution. *AIChE J.* **2000**, *46*, 1348−1367.

(6) Nguyen, T. D. From Formation Mechanisms to Synthetic Methods toward Shape-Controlled Oxide Nanoparticles. *Nanoscale* **2013**, *5*, 9455−9482.

(7) Marks, L. D.; Peng, L. Nanoparticle Shape, Thermodynamics and Kinetics. *J. Phys.: Condens. Matter* **2016**, *28*, No. 053001.

(8) Sekerka, R. F. Equilibrium and Growth Shapes of Crystals: How Do They Differ and Why Should We Care? *Cryst. Res. Technol.* **2005**, *40*, 291−306.

(9) Ringe, E.; Van Duyne, R. P.; Marks, L. D. Kinetic and Thermodynamic Modified Wulff Constructions for Twinned Nanoparticles. *J. Phys. Chem. C* **2013**, *117*, 15859−15870.

(10) Xia, Y.; Xiong, Y.; Lim, B.; Skrabalak, S. E. Shape-Controlled Synthesis of Metal Nanocrystals: Simple Chemistry Meets Complex Physics? *Angew. Chem., Int. Ed.* **2009**, *48*, 60−103.

(11) Kirkland, A. I.; Jefferson, D. A.; Duff, D. G.; Edwards, P. P.; Gameson, I.; Johnson, B. F. G.; Smith, D. J. Structural Studies of Trigonal Lamellar Particles of Gold and Silver. *Proc. R. Soc. London, Ser. A* **1993**, *440*, 589−609.

(12) Germain, V.; Li, J.; Ingert, D.; Wang, Z. L.; Pileni, M. P. Stacking Faults in Formation of Silver Nanodisks. *J. Phys. Chem. B* **2003**, *107*, 8717−8720.

(13) Xiong, Y.; Siekkinen, A. R.; Wang, J.; Yin, Y.; Kim, M. J.; Xia, Y. Synthesis of Silver Nanoplates at High Yields by Slowing Down the Polyol Reduction of Silver Nitrate with Polyacrylamide. *J. Mater. Chem.* **2007**, *17*, 2600−2602.

(14) Zhang, J.; Langille, M. R.; Mirkin, C. A. Photomediated Synthesis of Silver Triangular Bipyramids and Prisms: The Effect of pH and BSPP. *J. Am. Chem. Soc.* **2010**, *132*, 12502−12510.

(15) Ly, T.; Wen, J.; Marks, L. D. Kinetic Growth Regimes of Hydrothermally Synthesized Potassium Tantalate Nanoparticles. *Nano Lett.* **2018**, *18*, 5186−5191.

(16) Ly, T.; Wen, J.; Marks, L. D. Chemisorption-Driven Roughening of Hydrothermally Grown $KTa_{1-x}Nb_xO_3$ Nanoparticles. *J. Phys. Chem. C* **2020**, *124*, 7988−7993.

(17) Goh, G. K. L.; Haile, S. M.; Levi, C. G.; Lange, F. F. Hydrothermal Synthesis of Perovskite and Pyrochlore Powders of Potassium Tantalate. *J. Mater. Res.* **2002**, *17*, 3168−3176.

(18) *Mactempasx, version 2.3.44*; Total Resolution: Berkeley, 2019.

(19) Cowley, J. M.; Moodie, A. F. The Scattering of Electrons by Atoms and Crystals. I. A New Theoretical Approach. *Acta Crystallogr.* **1957**, *10*, 609−619.

(20) O'Keefe, M. A. *Proceedings of the 37th Annual Meeting of the Electron Microscopy Society of America, San Antonio, Texas, 1979*; Claitor's Publicating Division: Baton Rouge, 1979.

(21) Kohn, W.; Sham, L. J. Self-Consistent Equations Including Exchange and Correlation Effects. *Phys. Rev.* **1965**, *140*, A1133−A1138.

(22) Blaha, P.; Schwarz, K.; Madsen, G. K. H.; Kvasnicka, D.; Luitz, J.; Laskowski, R.; Tran, F.; Marks, L. D. *WIEN2k: An Augmented Plane Wave+Local Orbitals Program for Calculating Crystal Properties*; Vienna University of Technology: Austria, 2018.

(23) Blaha, P.; Schwarz, K.; Tran, F.; Laskowski, R.; Madsen, G. K. H.; Marks, L. D. WIEN2k: An APW+LO Program for Calculating the Properties of Solids. *J. Chem. Phys.* **2020**, *152*, No. 074101.

(24) Perdew, J. P.; Ruzsinszky, A.; Csonka, G. I.; Vydrov, O. A.; Scuseria, G. E.; Constantin, L. A.; Zhou, X.; Burke, K. Restoring the Density-Gradient Expansion for Exchange in Solids and Surfaces. *Phys. Rev. Lett.* **2008**, *100*, 136406.

(25) Magrez, A.; Vasco, E.; Seo, J. W.; Dieker, C.; Setter, N.; Forró, L. Growth of Single-Crystalline $KNbO_3$ Nanostructures. *J. Phys. Chem. B* **2006**, *110*, 58−61.

(26) Kumada, N.; Kyoda, T.; Yonesaki, Y.; Takei, T.; Kinomura, N. Preparation of $KNbO_3$ by Hydrothermal Reaction. *Mater. Res. Bull.* **2007**, *42*, 1856−1862.

(27) Simon, A.; Ravez, J. The Oxyfluoride Ferroelectrics. *Ferroelectrics* **2011**, *24*, 305−307.

(28) Kageyama, H.; Hayashi, K.; Maeda, K.; Attfield, J. P.; Hiroi, Z.; Rondinelli, J. M.; Poeppelmeier, K. R. Expanding Frontiers in Materials Chemistry and Physics with Multiple Anions. *Nat. Commun.* **2018**, *9*, 772.

(29) Harada, J. K.; Charles, N.; Poeppelmeier, K. R.; Rondinelli, J. M. Heteroanionic Materials by Design: Progress toward Targeted Properties. *Adv. Mater.* **2019**, *31*, 1805295.

(30) Huang, L.-F.; Koocher, N. Z.; Gu, M.; Rondinelli, J. M. Structure Dependent Phase Stability and Thermal Expansion of Ruddlesden−Popper Strontium Titanates. *Chem. Mater.* **2018**, *30*, 7100−7110.

(31) Udayakumar, K. R.; Cormack, A. N. Structural Aspects of Phase Equilibria in the Strontium-Titanium-Oxygen System. *J. Am. Ceram. Soc.* **1988**, *71*, C469−C471.

(32) McCoy, M. A.; Grimes, R. W.; Lee, W. E. Phase Stability and Interfacial Structures in the SrO−$SrTiO_3$ System. *Philos. Mag. A* **1997**, *75*, 833−846.

(33) Suzuki, T.; Fujimoto, M. First-Principles Structural Stability Study of Nonstoichiometry-Related Planar Defects in $SrTiO_3$ and $BaTiO_3$. *J. Appl. Phys.* **2001**, *89*, 5622−5629.

(34) Benavides, A. L.; Portillo, M. A.; Abascal, J. L. F.; Vega, C. Estimating the Solubility of 1:1 Electrolyte Aqueous Solutions: The Chemical Potential Difference Rule. *Mol. Phys.* **2017**, *115*, 1301−1308.

(35) Akerlof, G.; Bender, P. The Density of Aqueous Solutions of Potassium Hydroxide. *J. Am. Chem. Soc.* **1941**, *63*, 1085−1088.

(36) El Guendouzi, M.; Faridi, J. Thermodynamic Properties and Solubility of Potassium Fluoride in Aqueous Solutions at Various Temperatures. *J. Fluorine Chem.* **2020**, *235*, 109558.

(37) Jehng, J.-M.; Wachs, I. E. The Molecular Structures and Reactivity of Supported Niobidum Oxide Catalysts. *Catal. Today* **1990**, *8*, 37−55.

(38) Anderson, T. M.; Rodriguez, M. A.; Bonhomme, F.; Bixler, J. N.; Alam, T. M.; Nyman, M. An Aqueous Route to $[Ta_6O_{19}]^{8-}$ and Solid-State Studies of Isostructural Niobium and Tantalum Oxide Complexes. *Dalton Trans.* **2007**, 4517−4522.

(39) Deblonde, G. J. P.; Chagnes, A.; Bélair, S.; Cote, G. Solubility of Niobium(V) and Tantalum(V) under Mild Alkaline Conditions. *Hydrometallurgy* **2015**, *156*, 99−106.

(40) Balogh, E.; Anderson, T. M.; Rustad, J. R.; Nyman, M.; Casey, W. H. Rates of Oxygen-Isotope Exchange between Sites in the $[H_xTa_6O^{19}]^{(8-x)-}$(aq) Lindqvist Ion and Aqueous Solutions: Comparisons to $[H_xNb_6O_{19}]^{(8-x)-}$(aq). *Inorg. Chem.* **2007**, *46*, 7032−7039.

(41) Fullmer, L. B.; Molina, P. I.; Antonio, M. R.; Nyman, M. Contrasting Ion-Association Behaviour of Ta and Nb Polyoxometalates. *Dalton Trans.* **2014**, *43*, 15295−15299.

(42) Il'in, E. G.; Zozulin, A. N.; Buslaev, Y. A. 17O Nmr Estimation of Oxygen−Central Ion Bonding in the Products of Hydrolysis of Niobium, Tantalum, Arsenic, and Antimony Pentafluorides and the Symbatic Behavior of 17O and 19F NMR Chemical Shifts. *Dokl. Phys. Chem.* **2002**, *384*, 109−112.